

Chiral Terahertz Amplification and Lasing using Two-Dimensional Materials with Berry Curvature Dipole

Amin Hakimi^{1,*}, J. Sebastián Gómez-Díaz^{2,†} and Filippo Capolino^{1,‡}

¹ *Department of Electrical Engineering and Computer Science, University of California, Irvine, CA 92617, USA*

² *Department of Electrical and Computer Engineering, University of California, Davis, CA 95616, USA*

Compact, electrically driven sources of coherent terahertz (THz) radiation remain a challenge due to the lack of efficient gain media and scalable device platforms. Here, we propose and theoretically investigate a cavity-based THz gain mechanism enabled by Berry curvature dipole (BCD) in a DC-biased, low-symmetry two-dimensional (2D) material. Placing the biased 2D layer at the center of a Fabry-Pérot cavity enhances light-matter interactions, enabling direct conversion of DC electrical power into coherent THz radiation. We analyze the conditions for amplification and lasing, and identify the parameter regimes that support self-oscillatory coherent emission. Rather than introducing a specific device implementation, our work establishes the physical principles and operating conditions for BCD-enabled THz gain and lasing and provides the theoretical foundation for future realizations. The chiral nature of BCD-induced response enables bias-tunable chiral optical gain, selective polarization eigenstate amplification, and electrically controlled handedness of the emitted radiation. Importantly, substantial amplification and lasing are achieved using only a single 2D material, significantly simplifying device design while preserving scalability across the THz band via cavity-length tuning. This platform is broadly applicable to low-symmetry 2D materials with finite BCD, offering a general route toward compact, frequency-tunable, and polarization-selective THz sources.

keywords: Terahertz photonics, Berry curvature, Two-dimensional material, Electro-optic effect, Light-matter interaction

I. INTRODUCTION

Efficient and miniaturized sources of coherent radiation in the THz frequency range (0.1-10 THz) remain a critical challenge in modern photonics due to the so-called “THz gap”, stemming from the lack of natural gain media and efficient radiation mechanisms in this frequency band. Bridging this gap is crucial, as THz waves enable non-ionizing imaging for medical, security, and industrial applications, support sensitive molecular spectroscopy, and promise high-speed, short-range wireless communication beyond conventional microwave bandwidths [1–5]. Currently, THz generation relies on electronic, photonic, and quantum-based approaches. Electronic and optical methods typically use inefficient indirect mechanisms such as frequency mixing or difference-frequency generation [6] while semiconductor quantum devices enable direct emission, as the notable case of quantum cascade lasers (QCLs), operating primarily in the 1-5 THz range [7]. Despite their success, QCLs face intrinsic constraints including cryogenic operation, limited tunability, and millimeter-scale cavities [8, 9]. Consequently, the realization of room-temperature, broadband, coherent, and compact THz sources remains an open challenge [10–12]. Two-dimensional (2D) materials have recently offered a complementary approach to these conventional techniques, as their strong and unusual light-matter interactions and gate-tunable elec-

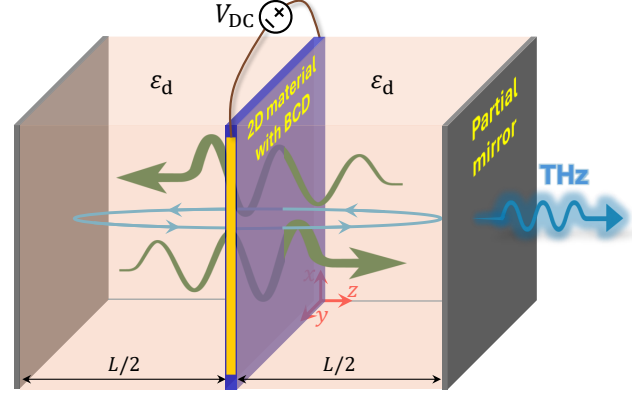


FIG. 1. Schematic of a cavity enhancing light-matter interactions in a DC-biased 2D material exhibiting BCD. The cavity is closed at both ends by partially reflecting mirrors.

tronic properties open unprecedented possibilities for the development of compact, tunable THz modulators, detectors, and emitters that will conform the next-generation of THz technologies [13–22].

In a related context, the geometry of electronic wavefunctions in solids, encoded in the Berry curvature, underpins many topological and nonlinear phenomena [23–25]. While often linked to time-reversal symmetry breaking, Berry curvature can be finite in nonmagnetic materials lacking inversion symmetry [26]. An asymmetric distribution of Berry curvature around the Fermi surface gives rise to the Berry curvature dipole (BCD), the first moment of the Berry curvature over occupied states [27], which signals geometric deformation in electronic bands and drives nonlinear quantum effects in

* amin.hakimi@uci.edu

† jsgomez@ucdavis.edu

‡ f.capolino@uci.edu

time-reversal-invariant systems. Materials with a finite BCD exhibit rich nonlinear electronic and optical responses, including the nonlinear Hall effect [28, 29], current rectification [30, 31], kinetic magnetoelectric effects [32, 33], and optical phenomena such as the circular photogalvanic and kinetic Faraday effects [34, 35], and enhanced second-harmonic generation [36]. Recent studies suggest that in low-symmetry 2D materials and non-centrosymmetric bulk materials, the BCD induces a non-Hermitian electro-optic (EO) response that generates a nonreciprocal optical gain dependent on light polarization and propagation direction [37–41]. Platforms such as twisted-bilayer graphene (TBG) [37, 38], WTe_2 [34, 42], twisted double bilayer graphene [43], and Weyl semimetals [44] are promising due to their large, tunable BCDs. Moreover, robust band structures can maintain large BCD even at room temperature [45]. Unlike conventional amplification relying on population inversion, this mechanism arises from intraband Bloch-electron dynamics under static fields [40, 46], where the optical wave drives electrons to emit additional in-phase radiation, conceptually akin to free-electron laser amplification [47].

Enhancing light-matter interactions strengthens the coupling between electromagnetic fields and material excitations. Engineered field enhancement via cavities, metasurfaces, or plasmonic structures has led to novel quantum and optoelectronic devices [48–52]. Here, we propose a cavity-based platform incorporating a single 2D material with BCD at its center to efficiently transfer energy from a DC bias into THz resonant modes. This DC-driven Fabry-Pérot (FP) cavity drastically enhances light-matter interactions on the 2D layer, increasing the overall THz amplification and enabling a frequency-tunable and scalable operation across the THz range. The chiral nature of the BCD-induced gain locks the handedness of the emitted light to the sign of the applied bias [38, 53]. Contrary to devices based on stacks of 2D materials [38], the proposed platform relies on a single 2D layer, which greatly simplifies its design and fabrication process and facilitates future experimental demonstrations. Rooted in a semi-classical Maxwellian formalism, we demonstrate that (i) THz amplification can be obtained and engineered even in the case of 2D layers with relatively large scattering rates; and (ii) damping mechanisms can be effectively mitigated by increasing the cavity quality factor, raising the DC bias, or operating at higher-order longitudinal cavity resonances. We further analyze the platform’s self-oscillatory lasing condition using complex-frequency analysis, identifying both the lasing threshold and the oscillatory frequency. Finally, we derive an analytical expression for the amplification threshold under high-frequency (low-loss) and low-frequency (high-loss) approximations, providing a practical guide to estimate the DC bias required to achieve THz amplification in practice. Cavity-based BCD platforms offer a practical route for tunable, scalable, and handedness-selective THz amplification and lasing.

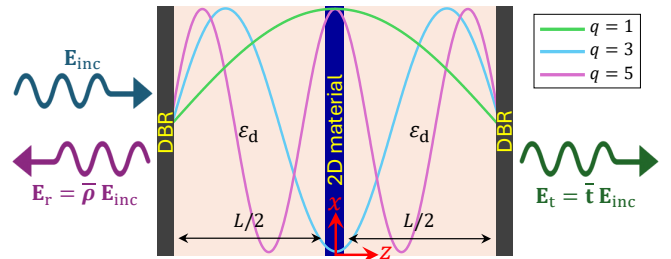


FIG. 2. Schematic of a Fabry-Pérot cavity enhancing light-matter interactions with a 2D material with BCD positioned at its center, and distributed Bragg reflectors (DBRs) placed at both ends acting as partially reflective mirrors. The longitudinal electric field profiles for odd-order resonances ($q = 1, 3, 5$) are shown, highlighting a field maximum at the cavity center. The 2D material with BCD is DC-biased, generating a transverse drift current resulting in optical chiral gain, with amplification controlled by the applied DC bias.

II. CAVITY MEDIATED AMPLIFICATION

In an ideal FP cavity with perfectly reflecting mirrors (i.e., reflection coefficient magnitude equal to unity), the allowed wavenumbers of the longitudinal cavity modes are $k_q = q\pi/L$, where $q = 1, 2, 3, \dots$ denotes the longitudinal mode index and L is the separation distance between the mirrors. For a cavity oriented along the z direction [54], the corresponding longitudinal electric field mode profiles take the form $\sin(k_q(z + L/2))$ for $-L/2 \leq z \leq L/2$, as illustrated in Fig. 2. These profiles exhibit alternating symmetry with respect to the cavity center ($z = 0$): mode profiles with odd q are symmetric and reach a maximum magnitude at the cavity center, whereas mode profiles with even q are antisymmetric and have a node (zero) at the cavity center.

Placing a 2D material capable of optical gain, such as TBG [37, 38], at the cavity center ($z = 0$) maximizes light-matter interactions and enables amplification of the odd cavity modes when sufficient gain is provided. Specifically, we propose the structure illustrated in Fig. 2, in which the 2D material is positioned at the center of the cavity to strongly interact with odd-order modes, and distributed Bragg reflectors (DBRs) are placed at both ends to serve as lossless partially reflective mirrors. By adjusting the cavity length, the supported odd modes can be engineered within the frequency range where TBG provides maximum amplification (0.1–4 THz), thereby achieving the highest possible amplification in the transmitted wave.

In the following, we develop a theoretical approach to explore the transmittance and reflectance spectra of the platform when it is excited by right- and left-circularly polarized (RCP and LCP) waves. Then, we evaluate amplification, gain, and the potential for lasing using a single TBG layer embedded in the FP cavity and examine the platform performance metrics versus the magnitude and sign of the BCD gain parameter, ξ .

A. Transfer Matrix Formulation

The transfer matrix method (TMM) provides a systematic framework to analyze the electromagnetic response of multilayered structures, and is especially useful for studying wave propagation, reflectance, transmittance, and absorbance in both periodic and non-periodic multilayer systems [55]. We begin by deriving the transfer matrix of a 2D material described by an anisotropic conductivity model, as illustrated in Fig. 3. In this work, the 2D material under consideration is TBG, whose conductivity matrix in the x, y basis is expressed as [37]

$$\bar{\sigma}(\omega) = \begin{bmatrix} \sigma_{xx} & \sigma_{xy} \\ \sigma_{yx} & \sigma_{xx} \end{bmatrix} = \frac{\sigma_0}{\gamma - i\omega} \begin{bmatrix} \omega_F & \xi \\ 0 & \omega_F \end{bmatrix} - \frac{\sigma_0}{\gamma} \begin{bmatrix} 0 & -\xi \\ \xi & 0 \end{bmatrix}, \quad (1)$$

where $\sigma_0 = 2e^2/h$ is the conductance quantum, $\gamma = 1/\tau$ is the scattering rate, and $\omega_F = E_F/\hbar$, with E_F denoting the Fermi level. The parameter ξ controls gain and rules the linear EO response; it is proportional to the applied static electric field E_0 and to the BCD of the material D_B : $\xi = \pi e D_B E_0/\hbar$, as described in [37, 38]. Note that ξ is a real-valued parameter, since both the applied DC field and D_B are real. However, depending on the orientation of the DC bias, ξ can take either positive or negative values.

The conductivity model described in Eq. (1) consists of two contributions. The first matrix represents the non-Hermitian component (i.e., neither purely Hermitian nor anti-Hermitian), which accounts for energy exchange between the 2D material and the interacting wave and can therefore lead to optical gain or loss. The second matrix represents the gyrotropic component of the conductivity, which is anti-Hermitian (skew-Hermitian), i.e., not associated with gain or loss, and is responsible for inducing nonreciprocity between the two polarization eigenstates of the electric field. The resulting eigenvalues of the conductivity matrix are

$$\sigma_{1,2} = \sigma_{xx} \mp \sqrt{\sigma_{xy}\sigma_{yx}}, \quad (2)$$

and the corresponding polarization eigenstates (eigenvectors) of the 2D material's conductivity are [38]

$$\mathbf{E}_{1,2}^\sigma = \begin{bmatrix} -i\sqrt{\frac{\omega+i2\gamma}{\omega+i\gamma}} \\ 1 \end{bmatrix}, \begin{bmatrix} i\sqrt{\frac{\omega+i2\gamma}{\omega+i\gamma}} \\ 1 \end{bmatrix}. \quad (3)$$

As discussed in [38], for a positive gain parameter $\xi > 0$, the eigenvalue σ_2 corresponds to a lossy polarization eigenstate, while σ_1 leads to gain when $\text{Re}(\sigma_1) < 0$. The amount of gain is controlled by the parameter ξ , which is responsible for the linear EO response. The polarization eigenstates have elliptical polarizations that become circular at high frequency when $\omega \gg \gamma$. However, in both the intermediate- and low-frequency regimes corresponding to large γ/ω , the modes are predominantly circularly polarized. Therefore, we employ circularly polarized waves as the incident excitation of the cavity (Fig. 2)

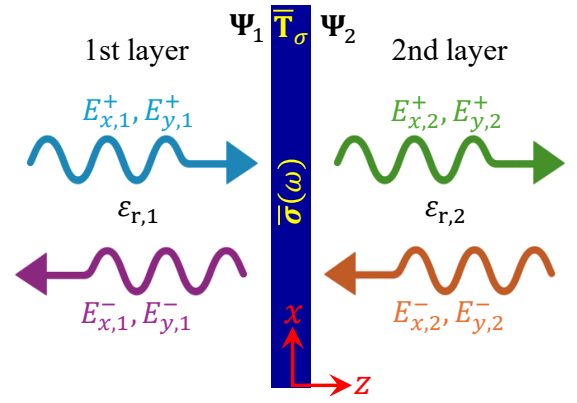


FIG. 3. Geometry of the structure used in the transfer-matrix derivation. A 2D material with surface conductivity $\bar{\sigma}(\omega)$ is sandwiched between two dielectric layers with different dielectric constants. Forward- and backward-propagating waves are shown on both sides of the 2D material.

to maximize light-matter interaction and achieve significant gain and amplification. Moreover, due to the chiral nature of the BCD-induced gain, the polarization eigenstate that exhibits gain can be selected by the sign of the parameter ξ . This results in chiral modes, which will be discussed in more detail in the context of the scattering and modal analysis of a cavity incorporating this 2D material. Notably, both the non-Hermitian and gyrotropic contributions to the conductivity are required to produce two distinct polarization eigenstates with nonreciprocal propagation: one experiencing gain and the other loss. Therefore, for positive ξ , the polarization eigenstate \mathbf{E}_1^σ is the one that can experience amplification, with opposite handedness when propagating either along the $+\hat{z}$ or $-\hat{z}$ direction.

In our theoretical framework, we adopt the time dependence convention $e^{-i\omega t}$, and fields are described by their phasors. The total electric field in the m -th dielectric layer is expressed as the superposition of forward- and backward-propagating plane waves, given by

$$\mathbf{E}_m = (E_{x,m}^+ \hat{\mathbf{x}} + E_{y,m}^+ \hat{\mathbf{y}}) e^{ikz} + (E_{x,m}^- \hat{\mathbf{x}} + E_{y,m}^- \hat{\mathbf{y}}) e^{-ikz}, \quad (4)$$

where $(E_{x,m}^+, E_{y,m}^+)$ and $(E_{x,m}^-, E_{y,m}^-)$ are complex amplitudes of the forward ($+\hat{z}$) and backward ($-\hat{z}$) waves, respectively. Then, the corresponding total magnetic field is given by

$$\mathbf{H}_m = \eta_m^{-1} (E_{x,m}^+ \hat{\mathbf{y}} - E_{y,m}^+ \hat{\mathbf{x}}) e^{ikz} - \eta_m^{-1} (E_{x,m}^- \hat{\mathbf{y}} - E_{y,m}^- \hat{\mathbf{x}}) e^{-ikz}, \quad (5)$$

where $\eta_m = \eta_0/\sqrt{\epsilon_{r,m}} = \sqrt{\mu_0/(\epsilon_0 \epsilon_{r,m})}$ is the wave impedance in the m -th dielectric layer with relative dielectric constant $\epsilon_{r,m}$. In our proposed platform, we consider a single 2D material placed at the center of the cavity ($z = 0$), sandwiched between two dielectric layers. Accordingly, we set $m = 1, 2$ in the following, as illustrated in Fig. 3.

By applying the electric and magnetic boundary conditions at the interface between the first and second layers, accounting for the presence of the anisotropic 2D material, and using the state vector in the m -th layer defined as $\Psi_m = [E_{x,m}^+, E_{y,m}^+, E_{x,m}^-, E_{y,m}^-]^T$, we obtain

$$\Psi_2 = \bar{\mathbf{T}}_\sigma \Psi_1, \quad (6)$$

where the forward transfer matrix of the 2D material, $\bar{\mathbf{T}}_\sigma$, is given by

$$\bar{\mathbf{T}}_\sigma = \frac{\eta_2}{2} \begin{bmatrix} (\eta_2^{-1} + \eta_1^{-1}) \bar{\mathbf{I}} - \bar{\boldsymbol{\sigma}} & (\eta_2^{-1} - \eta_1^{-1}) \bar{\mathbf{I}} - \bar{\boldsymbol{\sigma}} \\ (\eta_2^{-1} - \eta_1^{-1}) \bar{\mathbf{I}} + \bar{\boldsymbol{\sigma}} & (\eta_2^{-1} + \eta_1^{-1}) \bar{\mathbf{I}} + \bar{\boldsymbol{\sigma}} \end{bmatrix}, \quad (7)$$

where $\bar{\mathbf{I}}$ is the 2×2 identity matrix.

The transfer matrix representing wave propagation through a dielectric layer of dielectric constant ε_d and length $L/2$ represents wave propagation and is expressed as

$$\bar{\mathbf{T}}_d = \begin{bmatrix} e^{ik_d L/2} \bar{\mathbf{I}} & 0 \\ 0 & e^{-ik_d L/2} \bar{\mathbf{I}} \end{bmatrix}, \quad (8)$$

where $k_d = (\omega/c)\sqrt{\varepsilon_d} = k_0\sqrt{\varepsilon_d}$ is the wavenumber in that layer.

The transfer matrix of the lossless partially reflective mirrors terminating the cavity on both sides, modeled as DBR mirrors, is expressed as [56]

$$\bar{\mathbf{T}}_\rho = \frac{1}{\tau} \begin{bmatrix} (\tau^2 - \rho^2) \bar{\mathbf{I}} & \rho \bar{\mathbf{I}} \\ -\rho \bar{\mathbf{I}} & \bar{\mathbf{I}} \end{bmatrix}, \quad (9)$$

where $\rho = \rho_0 e^{i\theta_\rho}$, and $\tau = \sqrt{1 - \rho_0^2} e^{i(\theta_\rho \pm \pi/2)}$. Here, ρ is the field reflection coefficient, with magnitude ρ_0 and phase θ_ρ . Both choices of the \pm sign in the definition of τ are physically valid; however, since the cavity is terminated by two identical DBR mirrors, this sign choice does not affect the final total transfer matrix of the system.

Thus, for the structure illustrated in Fig. 2, the total transfer matrix is written as

$$\bar{\mathbf{T}}_{\text{tot}} = \bar{\mathbf{T}}_\rho \bar{\mathbf{T}}_d \bar{\mathbf{T}}_\sigma \bar{\mathbf{T}}_d \bar{\mathbf{T}}_\rho. \quad (10)$$

From this total transfer matrix, the reflection and transmission matrices are derived, allowing the calculation of reflectance and transmittance for any incident polarization. The total 4×4 transfer matrix $\bar{\mathbf{T}}_{\text{tot}}$ is partitioned into 2×2 submatrices as

$$\bar{\mathbf{T}}_{\text{tot}} = \begin{bmatrix} \bar{\mathbf{T}}_{11} & \bar{\mathbf{T}}_{12} \\ \bar{\mathbf{T}}_{21} & \bar{\mathbf{T}}_{22} \end{bmatrix}. \quad (11)$$

These submatrices form a system of equations relating the incident, reflected, and transmitted fields shown in Fig. 2, expressed as

$$\begin{bmatrix} \mathbf{E}_t \\ \mathbf{0} \end{bmatrix} = \begin{bmatrix} \bar{\mathbf{T}}_{11} & \bar{\mathbf{T}}_{12} \\ \bar{\mathbf{T}}_{21} & \bar{\mathbf{T}}_{22} \end{bmatrix} \begin{bmatrix} \mathbf{E}_{\text{inc}} \\ \mathbf{E}_r \end{bmatrix}. \quad (12)$$

By definition, the transmitted and reflected fields are related to the incident field as $\mathbf{E}_t = \bar{\mathbf{t}} \mathbf{E}_{\text{inc}}$ and $\mathbf{E}_r = \bar{\boldsymbol{\rho}} \mathbf{E}_{\text{inc}}$. Consequently, the reflection and transmission matrices are given by

$$\bar{\boldsymbol{\rho}} = -\bar{\mathbf{T}}_{22}^{-1} \bar{\mathbf{T}}_{21}, \quad (13)$$

$$\bar{\mathbf{t}} = \bar{\mathbf{T}}_{11} - \bar{\mathbf{T}}_{12} \bar{\mathbf{T}}_{22}^{-1} \bar{\mathbf{T}}_{21}. \quad (14)$$

Then, the reflectance and transmittance power for an incident wave \mathbf{E}_{inc} of arbitrary polarization are given by

$$\mathcal{T} = \frac{|\mathbf{E}_t|^2}{|\mathbf{E}_{\text{inc}}|^2} = \frac{\mathbf{E}_{\text{inc}}^\dagger \bar{\mathbf{T}} \mathbf{E}_{\text{inc}}}{\mathbf{E}_{\text{inc}}^\dagger \mathbf{E}_{\text{inc}}}, \quad (15)$$

$$\mathcal{R} = \frac{|\mathbf{E}_r|^2}{|\mathbf{E}_{\text{inc}}|^2} = \frac{\mathbf{E}_{\text{inc}}^\dagger \bar{\mathbf{R}} \mathbf{E}_{\text{inc}}}{\mathbf{E}_{\text{inc}}^\dagger \mathbf{E}_{\text{inc}}}, \quad (16)$$

Here, $\bar{\mathbf{T}} = \bar{\mathbf{t}}^\dagger \bar{\mathbf{t}}$ and $\bar{\mathbf{R}} = \bar{\boldsymbol{\rho}}^\dagger \bar{\boldsymbol{\rho}}$, where \dagger denotes the conjugate transpose. Consequently, absorptance is defined as $\mathcal{A} = 1 - \mathcal{R} - \mathcal{T}$. Having obtained the transmittance and reflectance of the structure shown in Fig. 2, we can evaluate the occurrence of amplification by analyzing how these quantities change with variations in the 2D material parameters. In particular, a negative absorptance indicates that the optical wave extracts energy from the 2D material, leading to optical amplification and gain.

B. Amplified Transmittance and Negative Absorptance

We evaluate the reflectance, transmittance, and absorptance of the structure shown in Fig. 2. Before presenting the results, we first determine an appropriate cavity length. According to the findings in [37], TBG exhibits its maximum amplification around 0.5 THz for $\gamma = 10^{12} \text{ s}^{-1}$ and around 1.5 THz for $\gamma = 5 \times 10^{12} \text{ s}^{-1}$. Therefore, we choose two FP cavity lengths such that the fundamental resonances correspond to these two frequencies. The resonant modes frequencies of an FP cavity of length L (without TBG layer in the middle) are given by $f_q = qv_p/(2L)$, where $v_p = c/\sqrt{\varepsilon_d}$ is the phase velocity in the dielectric medium inside the cavity. To place the fundamental resonance at 0.5 THz or 1.5 THz, the required cavity length is $L = c/(2f_1\sqrt{\varepsilon_d})$ where f_1 denotes the target fundamental resonance frequency of the FP cavity. For $\varepsilon_d = 4$, this yields $L = 149.90 \mu\text{m}$ for $f_1 = 0.5 \text{ THz}$ and $L = 49.96 \mu\text{m}$ for $f_1 = 1.5 \text{ THz}$.

The TBG parameters used in the analysis are $\omega_F/(2\pi) = 0.24 \text{ THz}$, $\gamma = 10^{12} \text{ s}^{-1}$, and the field reflection coefficient of the both DBRs is assumed to be $\rho = -0.9$, corresponding to $\rho_0 = 0.9$ with a constant phase $\theta_\rho = \pi$

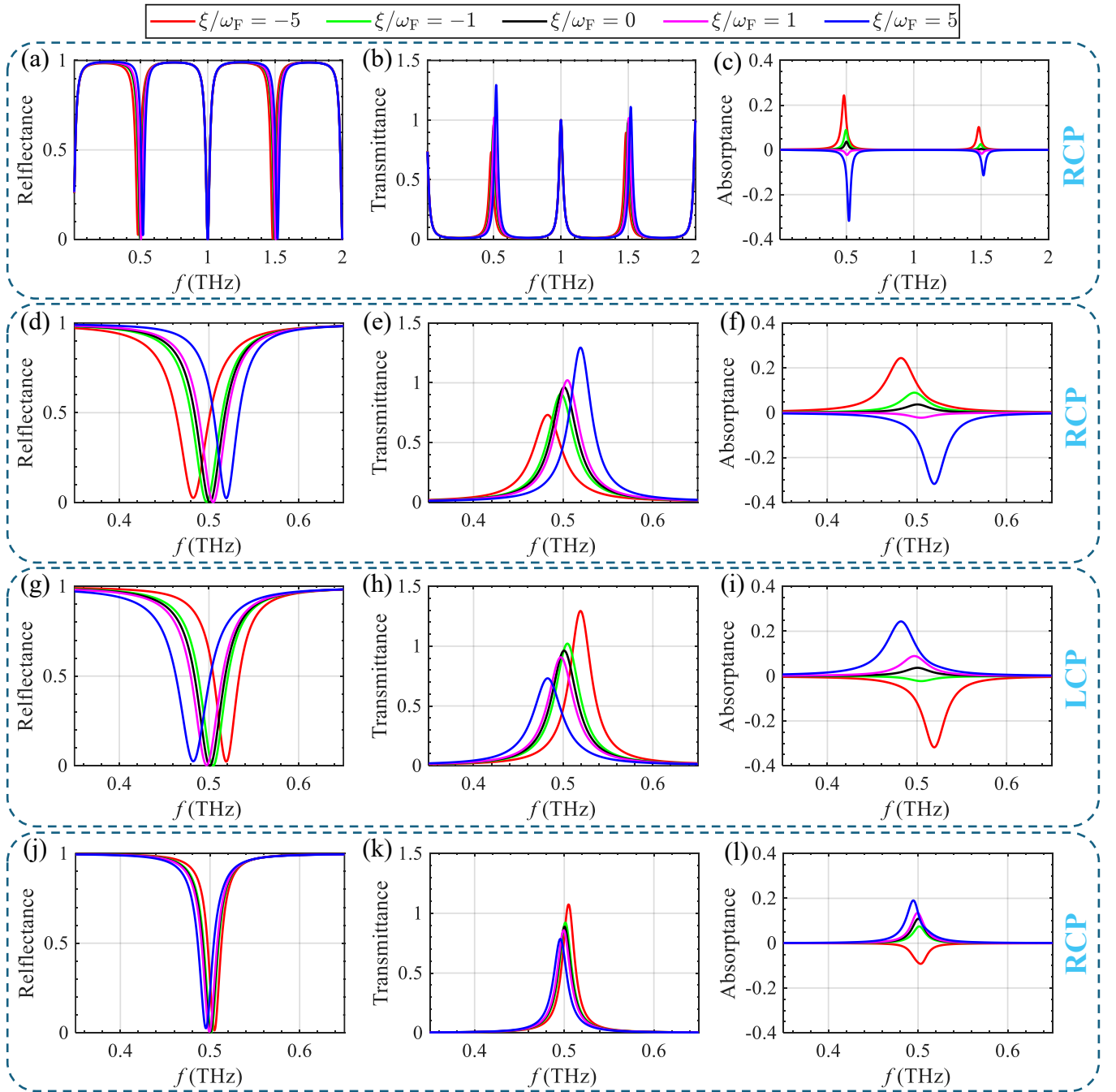


FIG. 4. Reflectance, transmittance, and absorbance of the platform proposed in Fig. 2 for various values of the gain parameter ξ of the TBG layer located at the center. DBR mirrors are at both ends as shown in Fig. 2. The first row (a–c) shows results for an RCP incident wave. The second row (d–f) provides a zoomed view near the fundamental resonance at 0.5 THz. The third row (g–i) presents the results for an LCP incident wave. The parameters for (a–i) are: $\varepsilon_d = 4$, $\omega_F/(2\pi) = 0.24$ THz, $\gamma = 10^{12} \text{ s}^{-1}$, $\rho = -0.9$, and $L = 149.90 \mu\text{m}$. The fourth row (j–l) corresponds to an RCP incident wave in the same cavity, but with increased TBG losses ($\gamma = 5 \times 10^{12} \text{ s}^{-1}$) and higher DBR reflectivity ($\rho = -0.95$). Amplification is seen in various cases.

(i.e. 90% field reflectivity). Note that transmittance values greater than unity or negative absorbance indicate gain, i.e., amplification of the propagating wave.

Fig. 4(a–c) (first row) presents the reflectance \mathcal{R} , transmittance \mathcal{T} , and absorbance \mathcal{A} of the structure shown in

Fig. 2 for an RCP incident wave from the left as the gain parameter ξ is varied. Throughout this paper, a circularly polarized incident wave traveling along $+\hat{z}$ is defined as $\mathbf{E}_{\text{inc}} = \frac{1}{\sqrt{2}} [1, \pm i]^T$, with the plus (minus) sign corresponding to RCP (LCP). It is observed that for all values

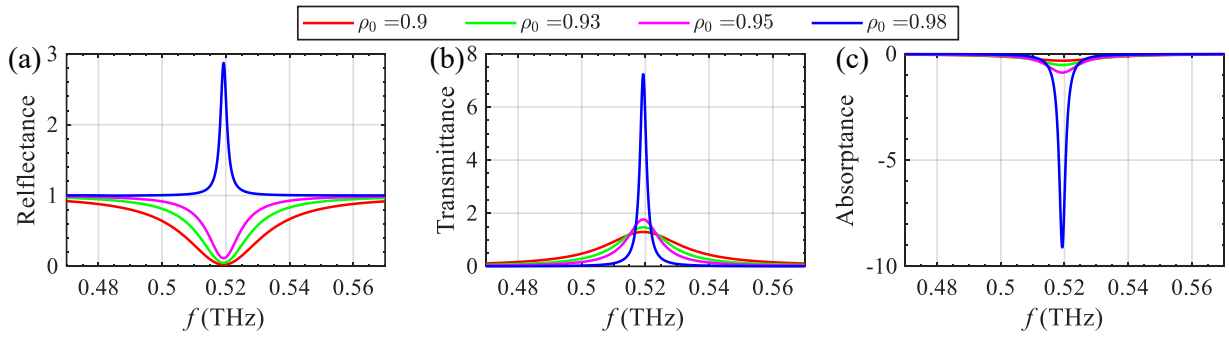


FIG. 5. (a) Reflectance, (b) transmittance, and (c) absorbance of the proposed FP cavity when it is illuminated by an RCP incident field. Results are plotted for various values of the DBRs' reflectivity coefficient ρ_0 . The parameters are: $\varepsilon_d = 4$, $\omega_F/(2\pi) = 0.24$ THz, $\gamma = 10^{12}$ s $^{-1}$, $\xi/\omega_F = 5$, and $L = 149.90$ μm .

of ξ there is no noticeable change around 1 THz and 2 THz, which correspond to the even-order resonances of the FP cavity, denoted by $q = 2$ and $q = 4$, respectively. As expected, the field profile of these modes is antisymmetric, resulting in an electric-field node at the cavity center, i.e., the standing wave does not interact with the 2D material located at the cavity center. As a result, no amplification or attenuation occurs with variations in ξ at those frequencies.

In contrast, around the odd-order resonances of the FP cavity (q odd), located around 0.5 THz ($q = 1$) and 1.5 THz ($q = 3$), amplification is observed for positive values of ξ and attenuation for negative values. Fig. 4(d-f) (second row) provides a closer view of the cavity response to RCP light near 0.5 THz. These plots reveal that increasing ξ enhances the gain and amplification of the transmitted wave. For positive ξ , the absorbance becomes negative, indicating that the 2D material provides energy to the light, and the transmittance exceeds unity, confirming amplification. It is important to emphasize that employing only a single TBG layer at the center of a cavity makes the proposed structure significantly simpler than the one presented in [38], where a stack of TBG layers was required to achieve comparable performance.

Figure 4(g-i) (third row) presents the same results for an incident wave with LCP. In this case, the results indicate that gain and amplification can be achieved for negative values of the parameter ξ . This demonstrates that by changing the sign of ξ , which corresponds to reversing the direction of the DC bias in the structure, the handedness of the amplified wave can be selected. This effect results in chiral light amplification, arising from the chiral nature of the gain, which is associated with the BCD in TBG. This feature highlights the tunability of our structure, enabling control over THz wave polarization. Furthermore, Fig. 4(j-l) (fourth row) shows the results for LCP when both losses and DBR reflectivity are increased. Specifically, the scattering rate is increased to $\gamma = 5 \times 10^{12}$ s $^{-1}$ and the reflectivity to $\rho = -0.95$. Larger losses reduce gain and amplification; however, the higher DBR reflectivity partly compensates by strength-

ening the cavity resonance. Also, increasing ξ to higher values can offset the effect of high losses, restoring amplification. Note that in all panels of Fig. 4, the cavity length is fixed at $L = 149.90$ μm .

Figure 5 shows the response as the magnitude of the DBR field reflectivity ρ_0 is varied while keeping the phase fixed at π . As seen, higher reflectivity significantly increases the transmittance and makes the absorbance more negative, indicating stronger light-matter interaction and an enhanced cavity effect. Interestingly, the reflectance also exhibits a degree of amplification for $\rho_0 = 0.98$. This enhancement further allows operation with larger loss values (γ) and smaller gain parameters (ξ), reducing the required DC bias applied to the 2D material.

Next, we examine how variations in the loss parameter γ affect the transmittance and gain of both the single TBG (no cavity) and TBG with cavity transmittance response. Figure 6 presents the transmittance and absorbance under RCP illumination from the left of the cavity, shown for three distinct loss parameters γ . Results in the first row (a,b) are for a TBG without a cavity, where the maximum amplification clearly depends on γ . In contrast, results in the second row (c,d) are for the TBG with cavity designed to have its first ($q = 1$) resonance near 0.5 THz, corresponding to $L = 149.90$ μm . Unlike the single TBG case, the resonance dictates the transmittance-peak frequency, so variations in γ do not significantly shift the frequency of maximum transmittance. As expected, an increased γ reduces the overall amplification. The third row (e,f) corresponds to the same cavity operating near the third resonance ($q = 3$). For small γ (red curve), the transmittance decreases relative to the fundamental resonance, consistent with the single-TBG behavior in the first row. However, when the loss is large (blue curve), the amplification is stronger at this third resonance than at the fundamental resonance.

The fourth row (g,h) shows results for a cavity designed to have the fundamental resonance near 1.5 THz, corresponding to $L = 49.96$ μm . These results mirror those of the third row but are spectrally expanded, illustrating

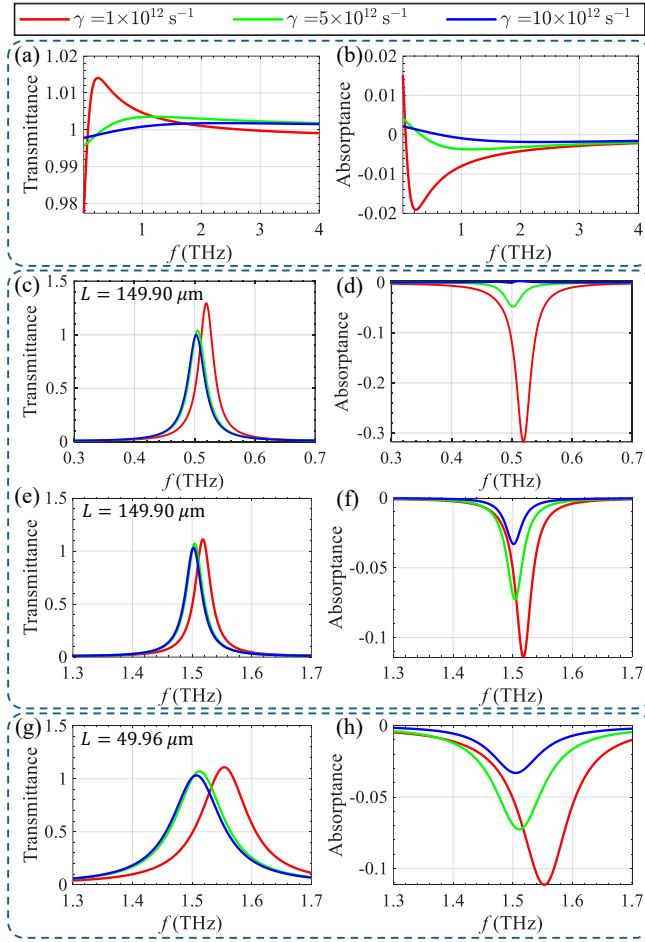


FIG. 6. Transmittance (left column) and absorbance (right column) of an electromagnetic structure that includes a TBG layer and is illuminated with an RCP wave. The structure is composed of (a,b) a single TBG in free-space; (c,d) the FP cavity shown in Fig. 2 with $L = 149.90 \mu\text{m}$, corresponding to having the first resonance ($q = 1$) near 0.5 THz; (e,f) the same cavity but observing frequencies near the third resonance ($q = 3$); (g,h) the FP cavity with $L = 49.96 \mu\text{m}$, observing frequencies near the fundamental resonance ($q = 1$). Other parameters are $\varepsilon_d = 4$, $\omega_F/(2\pi) = 0.24 \text{ THz}$, $\xi/\omega_F = 5$, and $\rho = -0.9$. Results are plotted for three distinct values of the loss parameter γ .

the scalability of the design with cavity length. Overall, variations in γ , cavity length, and mode index confirm that the proposed cavity exhibits robust and scalable performance.

To better understand the role of losses and to demonstrate that the cavity can still exhibit amplified transmittance at high scattering rates, we plot the transmittance as a function of frequency and gain parameter ξ for larger loss values in Fig. 7. Figure 7(a) shows that, for a moderate loss value of $\gamma = 5 \times 10^{12} \text{ s}^{-1}$, the amplification increases with the gain parameter around all odd-order resonances. However, the onset of amplified transmittance occurs at smaller ξ values around 1.5 THz compared to

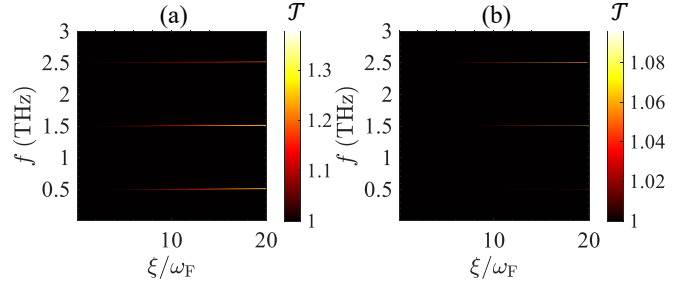


FIG. 7. Transmittance by varying frequency and gain parameter ξ/ω_F when (a) $\gamma = 5 \times 10^{12} \text{ s}^{-1}$, (b) $\gamma = 20 \times 10^{12} \text{ s}^{-1}$. Other parameters are $\varepsilon_d = 4$, $\omega_F/(2\pi) = 0.24 \text{ THz}$, $\rho = -0.9$, and $L = 149.90 \mu\text{m}$. For large losses γ , transmittance can still be larger than unity for resonances around 1.5 THz and 2.5 THz for a moderate value of the gain parameter.

the other resonances. In contrast, Fig. 7(b), corresponding to a higher loss value of $\gamma = 20 \times 10^{12} \text{ s}^{-1}$, shows that amplification occurs primarily around 1.5 and 2.5 THz, while amplification near 0.5 THz is observed only for very large values of the gain parameter. Moreover, the onset of amplification appears at a smaller ξ -threshold value for 2.5 THz, which corresponds to the higher odd-order longitudinal cavity mode ($q = 5$). These results indicate that, in general, as the loss parameter increases, higher odd-order longitudinal cavity modes are required to achieve the onset of amplification when tuning the gain parameter ξ .

The Supporting Information further validates the scalability and robustness of the cavity-TBG through a systematic optimization study, where the transmittance is mapped as a function of both cavity length and incident frequency for different loss values γ . In addition, the polarization of the transmitted wave is examined by evaluating the co- and cross-polarized field components versus frequency, gain, and loss parameters for both RCP and LCP incident waves. The cross-polarized component is found to be negligible, indicating that the cavity preserves the polarization of the incident wave. This means that the main function of cavity-TBG is amplification rather than polarization conversion, because the input polarization is maintained alongside scalable amplification.

In summary, analyzing the reflectance, transmittance, and absorbance of the structure shown in Fig. 2 reveals that, for an RCP incident wave from the left, the cavity can produce an amplified transmitted wave, with the level of amplification controlled by the parameter ξ , which is related to the applied DC bias on the 2D material. Furthermore, by reversing the sign of the applied bias, one can switch the amplification between the RCP and LCP incident waves. Also, if an RCP illuminates the cavity with TBG at its center from the right side, amplification for positive values of ξ would occur for LCP because of the chiral properties of TBG. Moreover, inherent losses in the 2D material reduce amplification, but this can be compensated by increasing the reflectivity of

the DBRs in the cavity, increasing the ξ , or operating at higher odd-order longitudinal cavity modes. Finally, it is worth noting that any low-symmetry 2D material exhibiting a BCD-induced gain could replace TBG in this configuration.

III. LASING CAVITY THRESHOLD

The reflectance, transmittance, and absorptance analysis presented in Section II showed that the 2D material with BCD can provide optical gain through its interaction with the intracavity field. Here, we focus on how gain enables the lasing condition. To this purpose, we perform a modal analysis to determine the eigenmodes of the cavity loaded with the 2D material at its center, as illustrated in Fig. 8. The complex-frequency resonance condition of the cavity is determined, and the lasing threshold is identified from the vanishing of the imaginary part of the complex frequency.

A. Complex-Frequency Resonance Condition

Let \mathbf{E} denote the electric field at an arbitrary position z inside the cavity. The resonance condition is given by

$$\bar{\rho}_r \bar{\rho}_l \mathbf{E} = \mathbf{E}, \quad (17)$$

where $\bar{\rho}_r$ and $\bar{\rho}_l$ are the reflection matrices looking to the right and to the left, respectively, evaluated at a chosen arbitrary z location. Here, we take this location to be immediately to the right of the 2D material, as illustrated in Fig. 8. Consequently, the resonance condition leads to

$$D(\omega) \equiv \det(\bar{\rho}_r \bar{\rho}_l - \bar{\mathbf{I}}) = 0. \quad (18)$$

The determination of $\bar{\rho}_r$ and $\bar{\rho}_l$ is detailed in the Supporting Information. Based on this analysis, the cavity resonances fall into two distinct classes, described by the following two conditions:

$$D_1(\omega) \equiv \sin(k_d L/2) = 0, \quad (19a)$$

and

$$D_2(\omega) \equiv \sigma_{xx} \mp \sqrt{\sigma_{xy}\sigma_{yx}} + i \frac{1}{\eta_d} \frac{1 - \cot^2(k_d L/2) + 2iy_m \cot(k_d L/2)}{iy_m - \cot(k_d L/2)} = 0, \quad (19b)$$

where $\eta_d = \eta_0/\sqrt{\varepsilon_d}$ is the characteristic wave impedance of the dielectric, and $y_m = (1 - \rho)/(1 + \rho)$ characterizes the reflectivity ρ of the partial mirror on the right side of the cavity, as illustrated in Fig. 8. In the limit $\rho \rightarrow -1$,

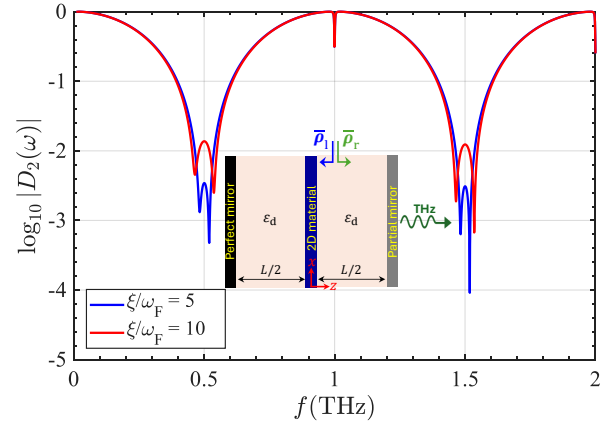


FIG. 8. Real-valued resonance frequencies given by the dips of $|D_2(\omega)|$ for two distinct values of ξ . To fully satisfy $D_2(\omega) = 0$ in Eq. (19b), f must be complex; however, the dips for real f in this plot approximate the cavity's oscillation frequencies. Parameters used are $\varepsilon_d = 4$, $\omega_F/(2\pi) = 0.24$ THz, $\gamma = 10^{12} \text{ s}^{-1}$, $L = 149.90 \mu\text{m}$, and $\rho = -0.99$, representing the field reflectivity of the partial mirror on the right. The inset depicts the proposed cavity configuration, as in Fig. 2, but terminated by a perfect (fully reflective) mirror on the left and a partially reflective mirror on the right.

the mirror becomes perfectly reflecting and y_m diverges to infinity. This modal analysis yields two distinct sets of cavity resonances. The first set, given by $D_1(\omega) = 0$ in Eq. (19a), corresponds to resonances with an anti-symmetric field profile. As discussed in Section II, these resonances exhibit a field node at the cavity center where the 2D material is placed. As a result, they experience neither amplification nor attenuation, since the field vanishes at the 2D layer and light-matter interactions are negligible.

We focus on the second set of resonances, given by $D_2(\omega) = 0$ in Eq. (19b). As discussed in Section II, these resonances exhibit an electric field maximum at the cavity center, thereby maximizing light-matter interaction. The resonance condition for these resonances yields two distinct branches, one associated with the minus sign (Mode 1, corresponding to the polarization eigenstate \mathbf{E}_1^σ in Eq. (3)) and the other with the plus sign (Mode 2, corresponding to the polarization eigenstate \mathbf{E}_2^σ in Eq. (3)). Similar to the modal analysis presented in [38], where a structure incorporating a stack of 2D material yielded two types of eigenmodes, one exhibiting optical gain and the other loss, here we also observe two different branches. One branch experiences optical gain, whereas the other experiences loss. The first two terms of $D_2(\omega)$ correspond to the eigenvalues of the conductivity matrix given in Eq. (2), corresponding to the two polarization eigenstates in Eq. (3). Clearly, the minus-sign branch (Mode 1) can produce a negative real part of the eigenvalue (when $\xi > 0$), which may lead to optical gain capable of compensating cavity losses and enabling lasing.

The dips in Figure 8 show the real-valued resonance frequencies obtained by plotting $|D_2(\omega)|$ versus real f , considering two distinct values of the gain parameters ξ . In particular, the dips correspond approximately to the real part of the complex-valued resonant frequencies of the cavity that fully satisfy $D_2(\omega) = 0$. Interaction between the optical wave propagating inside the cavity and the 2D material slightly shifts the resonance frequencies from the FP cavity resonances near 0.5 THz and 1.5 THz, due to the polarization eigenstate in Eq. (3) involved in the process. Near each of these frequencies, two distinct dips appear, corresponding to the minus-sign (Mode 1) and plus-sign (Mode 2) branches. The parameters used in this analysis are $\varepsilon_d = 4$, $\omega_F/(2\pi) = 0.24$ THz, $\gamma = 10^{12} \text{ s}^{-1}$, $L = 149.90 \mu\text{m}$, and a field reflection coefficient $\rho = -0.99$ for the partial mirror on the right side of the cavity shown in Fig. 8, corresponding to 99% reflectivity.

Having identified the frequencies of the cavity resonances interacting with the 2D material, we expect that Mode 1 (the minus-sign branch), which occurs at frequencies slightly above 0.5 THz and 1.5 THz, may exhibit amplification. In the next section, we verify this behavior by performing a complex frequency analysis. There, we also determine the lasing threshold—that is, the minimum value of the parameter ξ (corresponding to the applied bias) required to initiate lasing.

B. Lasing Threshold

The resonance frequencies obtained from Eq. (19b) and shown in Fig. 8 for various values of the ξ parameter are generally complex valued because they account for loss or gain in the system. Using the time-harmonic convention $e^{-i\omega t}$, a positive imaginary part of the complex frequency ($\text{Im}(f) > 0$) indicates an unstable, exponentially growing field, indicating optical amplification. The lasing threshold is found by setting $\text{Im}(f) = 0$, marking the transition from stability to instability.

Figure 9 shows the complex frequencies of the cavity resonances as the parameter ξ is varied over the range $1 < \xi/\omega_F < 15$. The top row presents the results near the fundamental resonance (around 0.5 THz, for $q = 1$) for two distinct values of loss γ , whereas the middle row corresponds to the second resonance (around 1.5 THz, for $q = 3$), both for $L = 149.90 \mu\text{m}$. The bottom row shows results around the fundamental resonance (around 1.5 THz, for $q = 1$) when $L = 49.96 \mu\text{m}$. In all panels, as expected, Mode 1, corresponding to the minus branch of Eq. (19b) and the polarization state \mathbf{E}_1^q in Eq. (3), exhibits instability (i.e., amplification) as ξ increases. The onset of lasing, indicated by the points where the curves intersect the $\text{Im}(f) = 0$ dashed line, is marked with cyan dots. These intersection points occur at $\xi_{\text{th}}/\omega_F = 2.41$ in (a), 10.78 in (b), 4.73 in (c), 7.40 in (d), 4.80 in (e), and 7.40 in (f), representing the minimum gain parameter required to initiate lasing for the given cavity lengths.

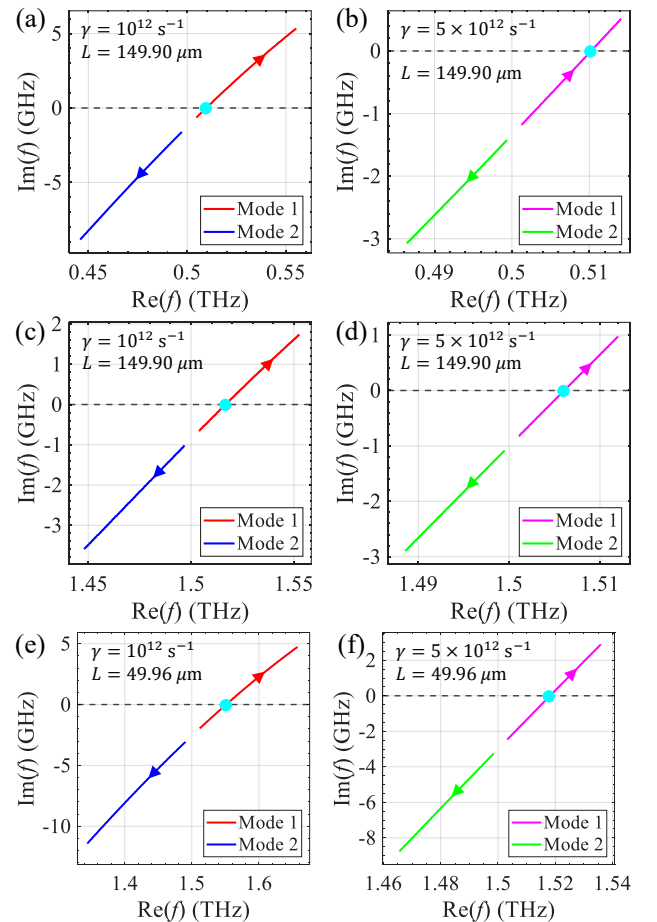


FIG. 9. Imaginary part versus real part of the lasing natural frequency as ξ/ω_F varies within $1 < \xi/\omega_F < 15$ [Solution to Eq. (19b)]. The top row shows the lasing around the fundamental resonance ($q = 1$), whereas the middle row shows lasing around the third resonance ($q = 3$), both for $L = 149.90 \mu\text{m}$. The bottom row shows lasing around the fundamental resonance ($q = 1$) for $L = 49.96 \mu\text{m}$. Panels (a), (c), and (e) correspond to $\gamma = 10^{12}$, while (b), (d), and (f) correspond to $\gamma = 5 \times 10^{12}$. Lasing occurs when $\text{Im}(f) > 0$, indicated by the intersections of the curves with the dashed line, marked by cyan dots.

Table I summarizes the corresponding lasing frequencies and gain thresholds for two γ values and two cavity lengths. Moreover, the required gain parameters for the middle and bottom two rows are nearly identical, despite the different cavity lengths and longitudinal resonance indices, $q = 3$ and $q = 1$, respectively. This behavior is consistent with the results in Fig. 6 (third and fourth rows), demonstrating the scalability and tunability of the proposed TBG-loaded cavity concept, where the lasing frequency, cavity length, and oscillating resonance-mode index q can be readily adjusted as desired. For large γ , the lasing threshold at the second resonance (near 1.5 THz) is lower than at the first resonance (near 0.5 THz).

Furthermore, polarization eigenstate 1 in Eq. (3) is responsible for amplification, consistent with Section II,

TABLE I. Minimum ξ required to initiate lasing and the corresponding lasing frequency for various loss values (γ) and cavity lengths (L). The superscript in approximated threshold values is computed using: (20a) or (20b).

L (μm)	γ (s^{-1})	f_r (THz)	ξ_{th}/ω_F	$\xi_{\text{th,a}}/\omega_F$
149.90	10^{12}	0.510	2.41	2.41 ^(20a)
	5×10^{12}	0.510	10.78	11.39 ^(20b)
	10^{12}	1.517	4.73	4.61 ^(20a)
	5×10^{12}	1.506	7.40	9.36 ^(20a)
49.96	10^{12}	1.551	4.80	4.61 ^(20a)
	5×10^{12}	1.518	7.40	9.36 ^(20a)

which predicts amplification for RCP when propagating along $+\hat{z}$ and for LCP when propagating along $-\hat{z}$ for $\xi > 0$. As a result, the intracavity eigenmode associated with lasing is the polarization eigenstate 1, and consequently, the emitted radiation, coming out from the right of the cavity shown in Fig. 8, is predominantly RCP. Notably, analogous to Section II, where changing the sign of ξ controls which handedness of the incident wave experiences amplification, here the sign of the applied DC bias can similarly control the handedness of the wave emitted from the lasing cavity. This feature enables the realization of a chiral THz lasing device.

We estimate the lasing threshold ξ_{th} analytically by applying suitable approximations to Eq. (19b). First, since the reflectivity of the cavity's right partial mirror is relatively high, we have $|y_m| \gg 1$. Additionally, the interaction between the cavity field and the 2D material slightly shifts the lasing frequency from the resonance of the unloaded FP cavity at 0.5 THz ($q = 1$) and 1.5 THz ($q = 3$). Assuming this shift to be small, we have $k_d L/2 \approx (2q - 1)\pi/2$ with $q = 1, 2, 3, \dots$, implying $|\cot(k_d L/2)| \ll 1$. The approximated threshold $\xi_{\text{th,a}}$ is found under two additional assumptions, $\omega \gg \gamma$ and $\omega \ll \gamma$, leading to, respectively:

$$\xi_{\text{th,a}}(\omega \gg \gamma) \approx 2 \left(\frac{\omega_{r,a}}{y_m \eta_d \sigma_0} + \gamma \frac{\omega_F}{\omega_{r,a}} \left(1 - \left(\frac{\gamma}{\omega_{r,a}} \right)^2 \right) \right) \left(1 - \frac{13}{8} \left(\frac{\gamma}{\omega_{r,a}} \right)^2 \right)^{-1} \quad (20a)$$

$$\xi_{\text{th,a}}(\omega \ll \gamma) \approx 2\sqrt{2} \frac{\gamma}{\omega_{r,a}} \left(\frac{\gamma}{y_m \eta_d \sigma_0} + \omega_F \left(1 - \left(\frac{\omega_{r,a}}{\gamma} \right)^2 \right) \right) \left(1 - \frac{25}{32} \left(\frac{\omega_{r,a}}{\gamma} \right)^2 \right)^{-1} \quad (20b)$$

Here, $\omega_{r,a} = (2q - 1)2\pi f_1$ is the approximate resonance angular frequency, assumed equal to that of the TBG-unloaded FP cavity. The full derivation of these expressions is provided in the Supporting Information. The last

column of Table I lists the $\xi_{\text{th,a}}$ values obtained using the approximate formulas in Eq. (20), based on the corresponding resonance frequency and loss values in each row. Comparison between the third column, which shows the exact gain parameter values, and the fourth column, which shows the approximate values, indicates very good agreement. The differences arise when the resonance angular frequency ω and loss γ are comparable, violating the assumption that one is much larger than the other. The approximate formulas in Eq. (20) provide a practical tool for estimating the required gain parameter, and consequently the necessary applied DC bias to the TBG, for the onset of lasing and optical amplification.

IV. CONCLUSION

We have proposed and theoretically analyzed a compact cavity architecture that enables direct terahertz amplification and lasing by DC electrical pumping of a low-symmetry 2D material with BCD. Embedding a biased 2D material in an FP cavity enhances light-matter interactions, enabling efficient conversion of DC bias into coherent THz radiation. Unlike conventional gain media, this approach does not rely on population inversion and instead exploits intraband Bloch-electron dynamics driven by BCD-induced chiral gain.

Using a transfer-matrix formalism and nonreciprocal modal analysis, we demonstrated selective amplification at the odd-order cavity resonances, negative absorptance, and transmittance exceeding unity, with gain controlled by the bias-dependent parameter ξ . We further showed that reversing the DC bias switches the handedness of the amplified or emitted radiation, enabling electrically tunable chiral THz operation. We also investigated the effect of 2D material losses and showed that, even under large intrinsic dissipation, the cavity and gain parameter can compensate for these losses and enable net THz amplification. Complex-frequency analysis revealed clear lasing thresholds for realistic material losses and mirror reflectivities. We derived approximate analytical expressions that accurately predict the gain threshold. Importantly, our results show that a single 2D material suffices to achieve substantial amplification and lasing, significantly simplifying the structure compared to multilayer designs previously analyzed while preserving strong performance and scalability across the THz band via cavity-length tuning.

In conclusion, this work establishes BCD-driven electro-optic gain in low-symmetry 2D materials as a viable mechanism for compact, electrically driven THz amplifiers and lasers that deserve to be further investigated in an experimental manner. Beyond TBG, the proposed platform is broadly applicable to a wide class of materials with BCD, providing a general route toward frequency-tunable, polarization-selective THz sources. The combination of compactness, frequency tunability, chiral control, and cavity-enhanced operation highlights the po-

tential of geometric electronic effects for integrated THz photonics, with promising implications for on-chip spec-

troscopy, sensing, and high-speed wireless communication.

-
- [1] A. G. Davies, E. H. Linfield, and M. B. Johnston, “The development of terahertz sources and their applications,” *Physics in Medicine & Biology*, vol. 47, no. 21, p. 3679, 2002.
- [2] M. Tonouchi, “Cutting-edge terahertz technology,” *Nature photonics*, vol. 1, no. 2, pp. 97–105, 2007.
- [3] A. Y. Pawar, D. D. Sonawane, K. B. Erande, and D. V. Derle, “Terahertz technology and its applications,” *Drug invention today*, vol. 5, no. 2, pp. 157–163, 2013.
- [4] T. Nagatsuma, G. Ducournau, and C. C. Renaud, “Advances in terahertz communications accelerated by photonics,” *Nature Photonics*, vol. 10, no. 6, pp. 371–379, 2016.
- [5] A. Leitenstorfer, A. S. Moskalenko, T. Kampfrath, J. Kono, E. Castro-Camus, K. Peng, N. Qureshi, D. Turchinovich, K. Tanaka, A. G. Markelz, *et al.*, “The 2023 terahertz science and technology roadmap,” *Journal of Physics D: Applied Physics*, vol. 56, no. 22, p. 223001, 2023.
- [6] M. Tymchenko, J. S. Gomez-Diaz, J. Lee, M. Belkin, and A. Alù, “Highly-efficient THz generation using nonlinear plasmonic metasurfaces,” *Journal of Optics*, vol. 19, no. 10, p. 104001, 2017.
- [7] L. Gao, C. Feng, and X. Zhao, “Recent developments in terahertz quantum cascade lasers for practical applications,” *Nanotechnology Reviews*, vol. 12, no. 1, p. 20230115, 2023.
- [8] M. A. Kainz, S. Schönhuber, A. M. Andrews, H. Detz, B. Limbacher, G. Strasser, and K. Unterrainer, “Barrier height tuning of terahertz quantum cascade lasers for high-temperature operation,” *ACS photonics*, vol. 5, no. 11, pp. 4687–4693, 2018.
- [9] C. Young, R. Cendejas, S. S. Howard, W. Sanchez-Vaynshteyn, A. J. Hoffman, K. J. Franz, Y. Yao, B. Mizaikoff, X. Wang, J. Fan, *et al.*, “Wavelength selection for quantum cascade lasers by cavity length,” *Applied Physics Letters*, vol. 94, no. 9, 2009.
- [10] Y.-S. Lee, *Principles of terahertz science and technology*, vol. 170. Springer Science & Business Media, 2009.
- [11] X.-C. Zhang, J. Xu, *et al.*, *Introduction to THz wave photonics*, vol. 29. Springer, 2010.
- [12] Y. Zhang, K. Li, and H. Zhao, “Intense terahertz radiation: generation and application,” *Frontiers of Optoelectronics*, vol. 14, no. 1, pp. 4–36, 2021.
- [13] P. Tassin, T. Koschny, and C. M. Soukoulis, “Graphene for terahertz applications,” *Science*, vol. 341, no. 6146, pp. 620–621, 2013.
- [14] M. Wang and E.-H. Yang, “THz applications of 2D materials: Graphene and beyond,” *Nano-structures & Nano-objects*, vol. 15, pp. 107–113, 2018.
- [15] J. Shi, Z. Li, D. K. Sang, Y. Xiang, J. Li, S. Zhang, and H. Zhang, “THz photonics in two dimensional materials and metamaterials: properties, devices and prospects,” *Journal of Materials Chemistry C*, vol. 6, no. 6, pp. 1291–1306, 2018.
- [16] K. Cong, E. Vetter, L. Yan, Y. Li, Q. Zhang, Y. Xiong, H. Qu, R. D. Schaller, A. Hoffmann, A. F. Kemper, *et al.*, “Coherent control of asymmetric spintronic terahertz emission from two-dimensional hybrid metal halides,” *Nature communications*, vol. 12, no. 1, p. 5744, 2021.
- [17] Q. Qiu and Z. Huang, “Photodetectors of 2D materials from ultraviolet to terahertz waves,” *Advanced Materials*, vol. 33, no. 15, p. 2008126, 2021.
- [18] L. Wang, N. Paul, J. Hihath, and J. Gomez-Diaz, “Giant and broadband THz and IR emission in drift-biased graphene-based hyperbolic nanostructures,” *Applied Physics Letters*, vol. 122, no. 19, 2023.
- [19] Y.-C. Lin, R. Torsi, R. Younas, C. L. Hinkle, A. F. Rigosi, H. M. Hill, K. Zhang, S. Huang, C. E. Shuck, C. Chen, *et al.*, “Recent advances in 2D material theory, synthesis, properties, and applications,” *ACS nano*, vol. 17, no. 11, pp. 9694–9747, 2023.
- [20] S. Pakniyat and J. S. Gomez-Diaz, “Magnet-free electromagnetic nonreciprocity in two-dimensional materials,” *Journal of Applied Physics*, vol. 136, no. 4, 2024.
- [21] Q. Guo, I. Esin, C. Li, C. Chen, G. Han, S. Liu, J. H. Edgar, S. Zhou, E. Demler, G. Refael, and F. Xia, “Hyperbolic phonon-polariton electroluminescence in 2D heterostructures,” *Nature*, vol. 639, pp. 915–921, 2025.
- [22] F. de Abajo, D. Basov, F. H. Koppens, L. Orsini, M. Cecanti, S. Castilla, L. Cavicchi, M. Polini, P. Gonçalves, A. Costa, *et al.*, “Roadmap for photonics with 2D materials,” *arXiv preprint arXiv:2504.04558*, 2025.
- [23] D. Xiao, M.-C. Chang, and Q. Niu, “Berry phase effects on electronic properties,” *Reviews of Modern Physics*, vol. 82, no. 3, pp. 1959–2007, 2010.
- [24] N. Nagaosa, J. Sinova, S. Onoda, A. H. MacDonald, and N. P. Ong, “Anomalous Hall effect,” *Reviews of Modern Physics*, vol. 82, no. 2, pp. 1539–1592, 2010.
- [25] A. Bansil, H. Lin, and T. Das, “Colloquium: Topological band theory,” *Reviews of Modern Physics*, vol. 88, no. 2, p. 021004, 2016.
- [26] D. Xiao, M.-C. Chang, and Q. Niu, “Berry phase effects on electronic properties,” *Reviews of Modern Physics*, vol. 82, no. 3, p. 1959, 2010.
- [27] I. Sodemann and L. Fu, “Quantum nonlinear Hall effect induced by Berry curvature dipole in time-reversal invariant materials,” *Physical Review Letters*, vol. 115, no. 21, p. 216806, 2015.
- [28] Z. Du, C. Wang, H.-Z. Lu, and X. Xie, “Band signatures for strong nonlinear Hall effect in bilayer WTe₂,” *Physical Review Letters*, vol. 121, no. 26, p. 266601, 2018.
- [29] Q. Ma, S.-Y. Xu, H. Shen, D. MacNeill, V. Fatemi, T.-R. Chang, A. M. Mier Valdivia, S. Wu, Z. Du, C.-H. Hsu, *et al.*, “Observation of the nonlinear Hall effect under time-reversal-symmetric conditions,” *Nature*, vol. 565, no. 7739, pp. 337–342, 2019.
- [30] D. Kumar, C.-H. Hsu, R. Sharma, T.-R. Chang, P. Yu, J. Wang, G. Eda, G. Liang, and H. Yang, “Room-temperature nonlinear Hall effect and wireless radiofrequency rectification in Weyl semimetal TaIrTe₄,” *Nature Nanotechnology*, vol. 16, no. 4, pp. 421–425, 2021.
- [31] S. Sinha, P. C. Adak, A. Chakraborty, K. Das, K. Deb-nath, L. V. Sangani, K. Watanabe, T. Taniguchi, U. V.

- Waghmare, A. Agarwal, *et al.*, “Berry curvature dipole senses topological transition in a moiré superlattice,” *Nature Physics*, vol. 18, no. 7, pp. 765–770, 2022.
- [32] T. Furukawa, Y. Shimokawa, K. Kobayashi, and T. Itou, “Observation of current-induced bulk magnetization in elemental tellurium,” *Nature Communications*, vol. 8, no. 1, p. 954, 2017.
- [33] F. Calavalle, M. Suárez-Rodríguez, B. Martín-García, A. Johansson, D. C. Vaz, H. Yang, I. V. Maznichenko, S. Ostanin, A. Mateo-Alonso, A. Chuvilin, *et al.*, “Gate-tunable and chirality-dependent charge-to-spin conversion in tellurium nanowires,” *Nature Materials*, vol. 21, no. 5, pp. 526–532, 2022.
- [34] S.-Y. Xu, Q. Ma, H. Shen, V. Fatemi, S. Wu, T.-R. Chang, G. Chang, A. M. M. Valdivia, C.-K. Chan, Q. D. Gibson, *et al.*, “Electrically switchable Berry curvature dipole in the monolayer topological insulator WTe₂,” *Nature Physics*, vol. 14, no. 9, pp. 900–906, 2018.
- [35] S. S. Tsirkin, P. A. Puente, and I. Souza, “Gyrotropic effects in trigonal tellurium studied from first principles,” *Physical Review B*, vol. 97, no. 3, p. 035158, 2018.
- [36] Q. Fu, X. Cong, X. Xu, S. Zhu, X. Zhao, S. Liu, B. Yao, M. Xu, Y. Deng, C. Zhu, *et al.*, “Berry curvature dipole induced giant mid-infrared second-harmonic generation in 2D Weyl semiconductor,” *Advanced Materials*, vol. 35, no. 46, p. 2306330, 2023.
- [37] T. G. Rappoport, T. A. Morgado, S. Lannebère, and M. G. Silveirinha, “Engineering transistorlike optical gain in two-dimensional materials with Berry curvature dipoles,” *Physical Review Letters*, vol. 130, no. 7, p. 076901, 2023.
- [38] A. Hakimi, K. Rouhi, T. G. Rappoport, M. G. Silveirinha, and F. Capolino, “Chiral terahertz lasing with Berry-curvature dipoles,” *Physical Review Applied*, vol. 22, no. 4, p. L041003, 2024.
- [39] T. A. Morgado, T. G. Rappoport, S. S. Tsirkin, S. Lannebère, I. Souza, and M. G. Silveirinha, “Non-hermitian linear electro-optic effect in three-dimensional materials,” *Physical Review B*, vol. 109, no. 24, p. 245126, 2024.
- [40] M. Eslami, A. Hakimi, L. A. Jauregui, and F. Capolino, “Berry curvature dipole-induced chiral terahertz gain and lasing in bulk tellurium,” *arXiv preprint arXiv:2508.18677*, 2025.
- [41] S. Lannebère, T. G. Rappoport, T. A. Morgado, I. Souza, and M. G. Silveirinha, “Symmetry analysis of the non-hermitian electro-optic effect in crystals,” *arXiv preprint arXiv:2502.03399*, 2025.
- [42] K. Kang, W. Zhao, Y. Zeng, K. Watanabe, T. Taniguchi, J. Shan, and K. F. Mak, “Switchable moiré potentials in ferroelectric WTe₂/WSe₂ superlattices,” *Nature Nanotechnology*, vol. 18, pp. 861–866, 2023.
- [43] D. de Sousa, N. Roldan-Levchenko, C. Ascencio, J. Forte, P. M. Haney, and T. Low, “Metallic electro-optic effect in twisted double-bilayer graphene,” *arXiv preprint arXiv:2510.23784*, 2025.
- [44] Y. Zhang, Y. Sun, and B. Yan, “Berry curvature dipole in Weyl semimetal materials: an ab initio study,” *Physical Review B*, vol. 97, no. 4, p. 041101, 2018.
- [45] T. Nishijima, T. Watanabe, H. Sekiguchi, Y. Ando, E. Shigematsu, R. Ohshima, S. Kuroda, and M. Shiraishi, “Ferroic Berry curvature dipole in a topological crystalline insulator at room temperature,” *Nano Letters*, vol. 23, no. 6, pp. 2247–2252, 2023.
- [46] N. Roldan-Levchenko, D. de Sousa, C. Ascencio, J. Forte, L. Martin-Moreno, and T. Low, “Optical gain through metallic electro-optical effects,” *arXiv preprint arXiv:2510.25659*, 2025.
- [47] P. G. O’Shea and H. P. Freund, “Free-electron lasers: Status and applications,” *Science*, vol. 292, no. 5523, pp. 1853–1858, 2001.
- [48] M. Ramezani, A. Halpin, A. I. Fernández-Domínguez, J. Feist, S. R.-K. Rodriguez, F. J. Garcia-Vidal, and J. Gómez Rivas, “Plasmon-exciton-polariton lasing,” *Optica*, vol. 4, no. 1, pp. 31–37, 2016.
- [49] P. Forn-Díaz, L. Lamata, E. Rico, J. Kono, and E. Solano, “Ultrastrong coupling regimes of light-matter interaction,” *Reviews of Modern Physics*, vol. 91, no. 2, p. 025005, 2019.
- [50] A. M. Berghuis, V. Serpenti, M. Ramezani, S. Wang, and J. Gomez Rivas, “Light-matter coupling strength controlled by the orientation of organic crystals in plasmonic cavities,” *The Journal of Physical Chemistry C*, vol. 124, no. 22, pp. 12030–12038, 2020.
- [51] L. Tao, Z. Chen, Z. Li, J. Wang, X. Xu, and J.-B. Xu, “Enhancing light-matter interaction in 2D materials by optical micro/nano architectures for high-performance optoelectronic devices,” *InfoMat*, vol. 3, no. 1, pp. 36–60, 2021.
- [52] K. Jo, E. Marino, J. Lynch, Z. Jiang, N. Gogotsi, T. P. Darlington, M. Soroush, P. J. Schuck, N. J. Borys, C. B. Murray, *et al.*, “Direct nano-imaging of light-matter interactions in nanoscale excitonic emitters,” *Nature Communications*, vol. 14, no. 1, p. 2649, 2023.
- [53] S. Lannebère, D. E. Fernandes, T. A. Morgado, and M. G. Silveirinha, “Chiral-gain photonics,” *Laser & Photonics Reviews*, vol. 19, no. 7, p. 2400881, 2025.
- [54] B. E. Saleh and M. C. Teich, *Fundamentals of photonics, 2 volume set*. John Wiley & Sons, 2019.
- [55] J. Hao and L. Zhou, “Electromagnetic wave scatterings by anisotropic metamaterials: Generalized 4×4 transfer-matrix method,” *Physical Review B—Condensed Matter and Materials Physics*, vol. 77, no. 9, p. 094201, 2008.
- [56] N. Furman, T. Mealy, M. S. Islam, I. Vitebskiy, R. Gibson, R. Bedford, O. Boyraz, and F. Capolino, “Frozen mode regime in an optical waveguide with a distributed bragg reflector,” *Journal of the Optical Society of America B*, vol. 40, no. 5, pp. 966–977, 2023.

Supporting Information:
Chiral Terahertz Amplification and Lasing
using Two-Dimensional Materials with Berry Curvature Dipole

SI. OPTIMAL AMPLIFICATION OPERATING POINT FOR CAVITY DESIGN

We aim to determine the optimal cavity length that maximizes amplification of the transmitted field as the frequency of the illuminating incident wave is varied, and for different values of the loss parameter γ . In addition, practical applications may require operation at different frequencies, motivating the need for a scalable cavity design. To address this, we calculate the transmittance of the cavity shown in Fig. 2 of the main body of the paper, under RCP illumination from the left, as a function of both the cavity length L and the illuminating frequency using Eq. (15) of the paper.

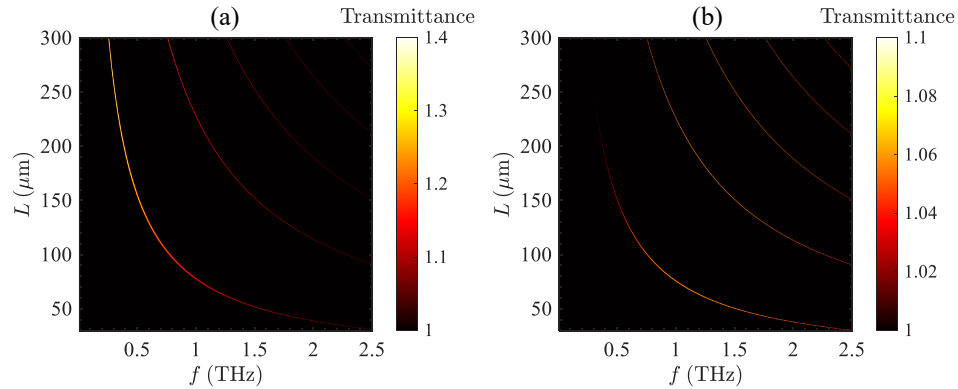


FIG. S1. Transmittance under RCP illumination from the left by varying cavity length and illuminating frequency for (a) $\gamma = 10^{12} \text{ s}^{-1}$, (b) $\gamma = 5 \times 10^{12} \text{ s}^{-1}$. The remaining parameters are $\varepsilon_d = 4$, $\omega_F/(2\pi) = 0.24 \text{ THz}$, $\xi/\omega_F = 5$, and $\rho = -0.9$.

Figure S1 presents the resulting transmittance maps for different values of γ . The contour lines indicate the combinations of frequency and cavity length that yield a transmittance greater than unity, with brighter contours corresponding to higher transmittance. We emphasize that this cavity design is general and can be applied to any 2D material exhibiting a non-Hermitian electro-optic response associated with a Berry curvature dipole that leads to gain and amplification, allowing similar optimization to identify the optimal operating point.

SII. POLARIZATION OF TRANSMITTED WAVES THROUGH THE CAVITY

We analyze the polarization of the field transmitted through the cavity shown in Fig. 2 of the main body of the paper. As explained there, the cavity is illuminated from the left with circularly polarized (CP) incident waves, and depending on the handedness of the incident wave, either the right- or left-circularly polarized (RCP and LCP) can exhibit amplified transmittance, which can be controlled by the direction of the applied DC bias. To this end, the transmitted electric field is first expressed as $\mathbf{E}_t = \bar{\mathbf{t}} \mathbf{E}_{\text{inc}}$, where $\bar{\mathbf{t}}$ is the transmission matrix of the cavity, defined in Eq. (14) of the paper. The transmitted electric field is then projected onto the RCP and LCP basis to extract the co- and cross-polarized components, yielding

$$E_t^{\text{co-pol}, \pm} = \left| \mathbf{e}_{\pm}^{\dagger} \bar{\mathbf{t}} \mathbf{e}_{\pm} \right|, \quad E_t^{\text{x-pol}, \pm} = \left| \mathbf{e}_{\mp}^{\dagger} \bar{\mathbf{t}} \mathbf{e}_{\pm} \right|, \quad (\text{S1})$$

where the \dagger denotes transpose conjugation. Here, (+) and (−) correspond to RCP and LCP, respectively, and $\mathbf{e}_{\pm} = \frac{1}{\sqrt{2}} [1, \pm i]^T$ denote the unit vectors associated with RCP (+) and LCP (−).

Figure S2 shows the co- and cross-polarization components of the transmitted field under RCP illumination for (top row) a twisted-bilayer graphene (TBG) *without* cavity, and (bottom row) a cavity with TBG at its center, for different values of the gain parameter ξ . Solid and dashed curves correspond to $\gamma = 10^{12} \text{ s}^{-1}$ and $\gamma = 5 \times 10^{12} \text{ s}^{-1}$, respectively. In the top row, the cross-polarization component is negligible compared to the co-polarization component, indicating that the polarization of the incident circularly polarized wave is largely preserved upon transmission through the

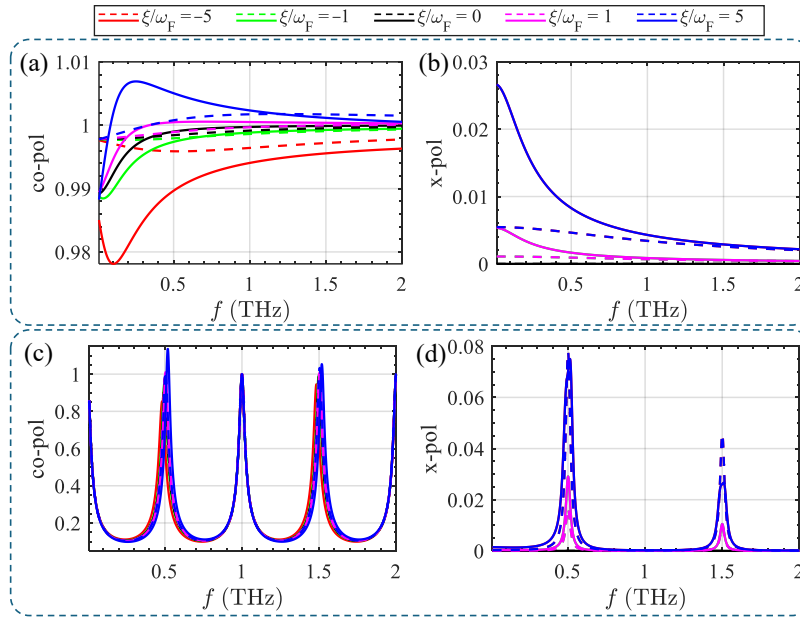


FIG. S2. Transmitted co- and cross-polarization components for RCP wave incidence on the TBG without (a,b) and with (c,d) cavity versus frequency for different values of the gain parameter ξ . Solid and dashed curves correspond to $\gamma = 10^{12} \text{ s}^{-1}$ and $\gamma = 5 \times 10^{12} \text{ s}^{-1}$, respectively. The other parameters are $\varepsilon_d = 4$, $\omega_F/(2\pi) = 0.24 \text{ THz}$. In (c,d), the cavity with TBG at its center has $L = 149.90 \mu\text{m}$ and $\rho = -0.9$. The incident field is coming from the left (see Fig. 2 of the main body of the paper); if it came from the right, amplification would occur for negative values of the gain parameter ξ .

single TBG, regardless of variations in the material parameters. In the bottom row, the co- and cross-polarization components for the designed cavity are shown. Here, the cross-polarization contribution is slightly increased due to the increased light-matter interaction provided by the cavity, which amplifies the intrinsic response of the 2D material. Nevertheless, the co-polarization component remains dominant, indicating that the transmitted wave retains the same polarization as the incident wave while experiencing significantly stronger amplification. Therefore, the proposed cavity design substantially enhances amplification without altering the polarization state of the incident wave.

In Fig. S2, the incident field is coming from the left (see Fig. 2 of the main body of the paper) with RCP polarization. For an LCP polarization incident from the left side, amplification would be observed for negative values of the gain parameter ξ . Since the same behavior would be observed for an LCP incident wave (except for a flip in the sign of ξ), these numerical results are omitted for brevity. Furthermore, if RCP is illuminating the TBG from the right side, amplification would occur for negative values of the gain parameter ξ due to the chiral properties of TBG.

III. DERIVATION OF RESONANCE CONDITION USING IMPEDANCE CONCEPT

We determine the reflection coefficient, which is essential for identifying the resonance condition in the cavity shown in Fig. S3. To this end, we model the structure using transmission-line theory, a powerful tool for describing *exactly* a large class of wave propagation and finding the reflection coefficient based on the impedance mismatch between different media. In this framework, the mirrors are represented as loads, and the 2D material at the center of the cavity is modeled as a shunt admittance. To obtain $\bar{\rho}_r$ and $\bar{\rho}_l$, we first calculate the admittances shown in Fig. S3. The admittance seen from the right, $Y_{\text{in},r}$, of a dielectric layer of length $L/2$ terminated by a partially reflective mirror is given by [S1]

$$Y_{\text{in},r} = Y_d \frac{Y_m - iY_d \tan(k_d L/2)}{Y_d - iY_m \tan(k_d L/2)}, \quad (\text{S2})$$

where $Y_d = Y_0 \sqrt{\varepsilon_d} = \sqrt{\varepsilon_0 \varepsilon_d / \mu_0}$ is the characteristic admittance of the dielectric layer, and Y_m is the admittance of the partially reflective mirror. For a partially reflective mirror with a desired field reflection coefficient ρ , the relation between ρ and Y_m is given by $\rho = (Y_d - Y_m) / (Y_d + Y_m)$. Accordingly, the corresponding load admittance Y_m (i.e., the admittance of the partially reflective mirror) is determined as

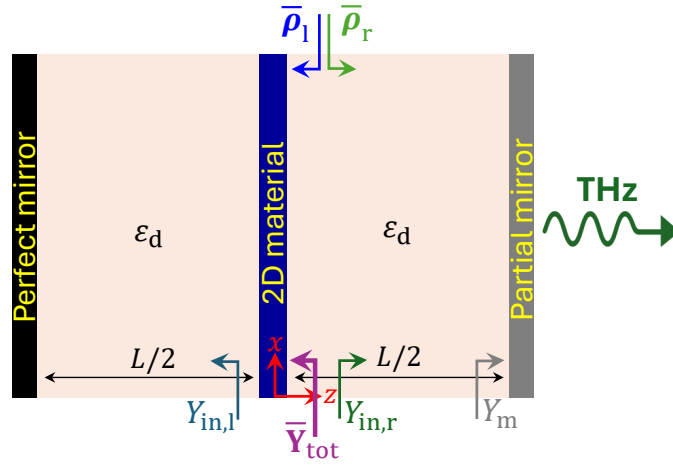


FIG. S3. Fabry-Pérot cavity with a 2D material exhibiting BCD positioned at the center to enhance light-matter interaction, terminated by a perfect mirror on one side and a partial mirror on the other to achieve THz lasing.

$$Y_m = Y_d \frac{1 - \rho}{1 + \rho} = y_m Y_d, \quad (\text{S3})$$

where $y_m = Y_m/Y_d = (1 - \rho)/(1 + \rho)$ denotes the normalized admittance of the partially reflective mirror seen from the cavity. Substituting this into Eq. (S2) yields

$$Y_{in,r} = Y_d \frac{y_m - i \tan(k_d L/2)}{1 - i y_m \tan(k_d L/2)}. \quad (\text{S4})$$

On the left side of the 2D material, the admittance $Y_{in,r}$ is seen toward the left of the dielectric layer of length $L/2$ terminated by a perfect (fully reflective) mirror. Here, we consider the perfect mirror as a perfect electric conductor (PEC), i.e., a short circuit. Accordingly, the input admittance in configuration $Y_{in,l}$ is given by [S1]

$$Y_{in,l} = i Y_d \cot(k_d L/2). \quad (\text{S5})$$

The 2D material is placed in parallel with $Y_{in,l}$, as shown in Fig. S3. Thus, the total admittance \bar{Y}_{tot} is

$$\bar{Y}_{tot} = Y_{in,l} \bar{\mathbf{I}} + \bar{\boldsymbol{\sigma}}, \quad (\text{S6})$$

where $\bar{\boldsymbol{\sigma}}$ is the conductivity tensor of the TBG given in Eq. (1) of the paper. Then, using the admittances derived above, the reflection coefficients $\bar{\rho}_r$ and $\bar{\rho}_l$ are expressed as

$$\bar{\rho}_l = (\bar{Y}_d + \bar{Y}_{tot})^{-1} (\bar{Y}_d - \bar{Y}_{tot}), \quad (\text{S7})$$

$$\bar{\rho}_r = (\bar{Y}_d + \bar{Y}_{in,r})^{-1} (\bar{Y}_d - \bar{Y}_{in,r}), \quad (\text{S8})$$

with $\bar{Y}_{in,r} = Y_{in,r} \bar{\mathbf{I}}$, and $\bar{Y}_d = Y_d \bar{\mathbf{I}}$. Then, $\bar{\rho}_l$ is simplified as,

$$\bar{\rho}_r = \frac{Y_d - Y_{in,r}}{Y_d + Y_{in,r}} \bar{\mathbf{I}} = \frac{1 - y_m}{1 + y_m} \exp(ik_d L) \bar{\mathbf{I}} = \Gamma_r \bar{\mathbf{I}}. \quad (\text{S9})$$

With these definitions, the resonance condition obtained in the paper $D(\omega) \equiv \det(\bar{\rho}_r \bar{\rho}_l - \bar{\mathbf{I}}) = 0$, simplifies to

$$\frac{[(1 + \Gamma_r) \sigma_{xx} + (Y_+ - \Gamma_r Y_-)]^2 - (1 + \Gamma_r)^2 \sigma_{xy} \sigma_{yx}}{(\sigma_{xx} + Y_+)^2 - \sigma_{xy} \sigma_{yx}} = 0, \quad (\text{S10})$$

where

$$Y_+ = Y_d + Y_{\text{in},1} = Y_d (1 + i \cot(k_d L/2)) = i Y_d \csc(k_d L/2) \exp(-i k_d L/2), \quad (\text{S11})$$

$$Y_- = Y_d - Y_{\text{in},1} = Y_d (1 - i \cot(k_d L/2)) = -i Y_d \csc(k_d L/2) \exp(i k_d L/2). \quad (\text{S12})$$

The resonance condition is satisfied either when the numerator of Eq. (S10) becomes zero or when its denominator diverges to infinity. From Eq. (S11), the denominator diverges when

$$D_1(\omega) \equiv \sin(k_d L/2) = 0, \quad (\text{S13})$$

corresponding to antisymmetric resonance-mode profiles with an electric field node at the cavity center; whereas, the resonances arising from the zeros of the numerator satisfy

$$D_2(\omega) \equiv \sigma_{xx} \mp \sqrt{\sigma_{xy}\sigma_{yx}} + \frac{Y_+ - \Gamma_r Y_-}{1 + \Gamma_r} = 0. \quad (\text{S14})$$

The resonances of $D_1(\omega) = 0$ are related to the even-order resonances of the FP cavity discussed in the paper. We now focus on the resonances arising from the zeros of the numerator $D_2(\omega) = 0$, which correspond to the odd-order resonances. This relation is further simplified using Eqs. (S11) and (S12). The $-$ and $+$ signs correspond to the polarization eigenstates \mathbf{E}_1^σ and \mathbf{E}_2^σ in Eq. (3) of the main body of the paper, respectively. Assuming $Y_d = 1/\eta_d$, the final resonance condition for the odd-order FP resonances becomes

$$D_2(\omega) \equiv \sigma_{xx} \mp \sqrt{\sigma_{xy}\sigma_{yx}} + i \frac{1}{\eta_d} \frac{1 - \cot^2(k_d L/2) + 2i y_m \cot(k_d L/2)}{i y_m - \cot(k_d L/2)} = 0. \quad (\text{S15})$$

SIV. DERIVATION OF LASING THRESHOLD

We aim to determine the threshold value of the gain parameter (ξ) corresponding to the onset of lasing. We start from the dispersion equation for the resonances interacting with the 2D material (odd-order FP resonances), given in Eq. (S15),

$$\sigma_{xx} \mp \sqrt{\sigma_{xy}\sigma_{yx}} + i \frac{1}{\eta_d} \frac{1 - \cot^2(k_d L/2) + 2i y_m \cot(k_d L/2)}{i y_m - \cot(k_d L/2)} = 0. \quad (\text{S16})$$

Assuming that the cavity resonance frequency is close to that of the unloaded FP cavity and that the frequency shift due to interaction with the 2D material is small, we have $k_d L/2 \approx (2q - 1)\pi/2$ with $q = 1, 2, 3, \dots$, which implies $|\cot(k_d L/2)| \ll 1$, where q is the FP resonance index. Since this dispersion equation corresponds to odd-order resonances, only odd integers $(2q - 1)$ are considered. In addition, the partial mirror on the right side of the cavity (Fig. S3) is assumed to have high reflectivity with a constant phase of π , i.e., a reflection coefficient close to -1 , which leads to $|y_m| \gg 1$. Under these approximations, the dispersion equation is simplified as

$$\sigma_{xx} \mp \sqrt{\sigma_{xy}\sigma_{yx}} + i \frac{1}{\eta_d} \frac{1 + 2i y_m \cot(k_d L/2)}{i y_m} \approx 0. \quad (\text{S17})$$

After straightforward algebraic manipulation and using the trigonometric identity to express $\cot(\cdot)$ to $\tan(\cdot)$, the dispersion relation reduces to

$$\sigma_{xx} \mp \sqrt{\sigma_{xy}\sigma_{yx}} + i \frac{1}{\eta_d} \left(-i y_m^{-1} + 2 \tan \left(\frac{(2q - 1)\pi}{2} - \frac{k_d L}{2} \right) \right) \approx 0. \quad (\text{S18})$$

Assuming the cavity resonance remains close to that of the FP cavity without TBG, the argument of the $\tan(\cdot)$ function is close to zero, allowing us to use the first-order Taylor expansion of $\tan(\cdot)$. Under this approximation, the dispersion relation becomes

$$\sigma_{xx} \mp \sqrt{\sigma_{xy}\sigma_{yx}} \approx i \frac{1}{\eta_d} (i y_m^{-1} + (k_d L - (2q - 1)\pi)). \quad (\text{S19})$$

The left-hand side of the above equation corresponds to the eigenvalues $\sigma_{1,2}$ of the conductivity matrix $\bar{\sigma}$, given in Eq. (2) of the paper, associated with the polarization eigenstates $\mathbf{E}_{1,2}^\sigma$ in Eq. (3) of the paper. Since we are interested in the lasing threshold, only the polarization eigenstate that exhibits gain (polarization eigenstate 1, when $\xi > 0$) is relevant; therefore, we consider only σ_1 that has the negative sign. Conversely, when $\xi < 0$, polarization eigenstate 2 is the one that experiences gain.

These eigenvalues are approximated in two distinct regimes, determined by the comparison between the operating angular frequency ω and losses γ . In particular, we consider: (i) the high-frequency, low-loss regime ($\omega \gg \gamma$), and (ii) the low-frequency, high-loss regime ($\omega \ll \gamma$). In each regime, we employ a Taylor series expansion to approximate the eigenvalue of the conductivity matrix, which simplifies the left-hand side of the above equation. First, when $\omega \gg \gamma$, we obtain

$$\sigma_{xx} - \sqrt{\sigma_{xy}\sigma_{yx}} \approx i\sigma_0 \left[\left(\frac{\omega_F}{\omega} + \frac{\xi}{\gamma} \right) + i\frac{\gamma}{\omega} \left(-\frac{\omega_F}{\omega} + \frac{\xi}{2\gamma} \right) + \left(\frac{\gamma}{\omega} \right)^2 \left(-\frac{\omega_F}{\omega} + \frac{5\xi}{8\gamma} \right) + i\left(\frac{\gamma}{\omega} \right)^3 \left(\frac{\omega_F}{\omega} - \frac{13\xi}{16\gamma} \right) \right]. \quad (\text{S20})$$

Substituting this approximation into Eq. (S19) yields

$$i\sigma_0 \left[\left(\frac{\omega_F}{\omega} + \frac{\xi}{\gamma} \right) + i\frac{\gamma}{\omega} \left(-\frac{\omega_F}{\omega} + \frac{\xi}{2\gamma} \right) + \left(\frac{\gamma}{\omega} \right)^2 \left(-\frac{\omega_F}{\omega} + \frac{5\xi}{8\gamma} \right) + i\left(\frac{\gamma}{\omega} \right)^3 \left(\frac{\omega_F}{\omega} - \frac{13\xi}{16\gamma} \right) \right] \approx i\frac{1}{\eta_d} (iy_m^{-1} + (k_d L - (2q - 1)\pi)) \quad (\text{S21})$$

Rewriting this equation by separating the real and imaginary parts, we obtain

$$\begin{aligned} & \left[\eta_d \sigma_0 \left(\left(\frac{\omega_F}{\omega} + \frac{\xi}{\gamma} \right) + \left(\frac{\gamma}{\omega} \right)^2 \left(-\frac{\omega_F}{\omega} + \frac{5\xi}{8\gamma} \right) \right) + (2q - 1)\pi - \frac{\omega}{2f_1} \right] + \\ & i \left[\eta_d \sigma_0 \left(\frac{\gamma}{\omega} \left(-\frac{\omega_F}{\omega} + \frac{\xi}{2\gamma} \right) + \left(\frac{\gamma}{\omega} \right)^3 \left(\frac{\omega_F}{\omega} - \frac{13\xi}{16\gamma} \right) \right) - y_m^{-1} \right] \approx 0. \end{aligned} \quad (\text{S22})$$

By solving this complex-valued equation for ω , we can determine the complex lasing frequency and the corresponding required gain parameter. Under the time-evolution convention $e^{-i\omega t}$ adopted here, lasing occurs when $\text{Im}(\omega) > 0$. Therefore, the lasing threshold corresponds to the point at which the complex frequency crosses the real axis in the complex- ω plane, indicating the onset of lasing. Both the real and imaginary parts of Eq. (S22) must simultaneously vanish at this crossing, resulting in a coupled system of two equations for real ω and ξ . The real part is primarily important to determine the lasing frequency, which remains close to the unloaded FP cavity resonance because $\eta_d \sigma_0 \ll 1$. Consequently, the lasing threshold condition is well approximated by requiring only the imaginary part of Eq. (S22) to vanish:

$$\eta_d \sigma_0 \left(\frac{\gamma}{\omega} \left(-\frac{\omega_F}{\omega} + \frac{\xi}{2\gamma} \right) + \left(\frac{\gamma}{\omega} \right)^3 \left(\frac{\omega_F}{\omega} - \frac{13\xi}{16\gamma} \right) \right) - y_m^{-1} \approx 0. \quad (\text{S23})$$

Here, ω must be specified to determine the corresponding value of ξ . We take $\omega \approx (2q - 1)2\pi f_1 \equiv \omega_{r,a}$, which is the approximate resonance angular frequency, assumed equal to that of the TBG-unloaded FP cavity. Finally, the corresponding approximate gain parameter $\xi_{\text{th},a}$ required for the onset of lasing when $\omega \gg \gamma$ is obtained as

$$\xi_{\text{th},a}(\omega \gg \gamma) \approx 2 \left(\frac{\omega_{r,a}}{y_m \eta_d \sigma_0} + \gamma \frac{\omega_F}{\omega_{r,a}} \left(1 - \left(\frac{\gamma}{\omega_{r,a}} \right)^2 \right) \right) \left(1 - \frac{13}{8} \left(\frac{\gamma}{\omega_{r,a}} \right)^2 \right)^{-1}. \quad (\text{S24})$$

Then, the same analysis is carried out for $\omega \ll \gamma$. In this case, the approximate eigenvalue of the conductivity is obtained as

$$\sigma_{xx} - \sqrt{\sigma_{xy}\sigma_{yx}} \approx i\sigma_0 \left[\left(-i\frac{\omega_F}{\gamma} + \frac{\sqrt{2\xi}}{\gamma} \right) + \frac{\omega}{\gamma} \left(\frac{\omega_F}{\gamma} + i\frac{\sqrt{2\xi}}{4\gamma} \right) + \left(\frac{\omega}{\gamma} \right)^2 \left(i\frac{\omega_F}{\gamma} - \frac{7\sqrt{2\xi}}{32\gamma} \right) + \left(\frac{\omega}{\gamma} \right)^3 \left(-\frac{\omega_F}{\gamma} - i\frac{25\sqrt{2\xi}}{128\gamma} \right) \right]. \quad (\text{S25})$$

Following the same procedure as in the previous case, the corresponding approximate gain parameter $\xi_{\text{th},a}$ required for the onset of lasing when $\omega \ll \gamma$ is obtained as

$$\xi_{\text{th,a}}(\omega \ll \gamma) \approx 2\sqrt{2} \frac{\gamma}{\omega_{\text{r,a}}} \left(\frac{\gamma}{y_{\text{m}}\eta_{\text{d}}\sigma_0} + \omega_{\text{F}} \left(1 - \left(\frac{\omega_{\text{r,a}}}{\gamma} \right)^2 \right) \right) \left(1 - \frac{25}{32} \left(\frac{\omega_{\text{r,a}}}{\gamma} \right)^2 \right)^{-1}. \quad (\text{S26})$$

[S1] D. M. Pozar, *Microwave Engineering* (John Wiley & Sons, 2009) Chap. 2.